

Development of a high-fidelity computational tool for chemically reacting hypersonic flow simulations

Athanasios T. Margaritis^{1,4*}, Clément Scherding², Olaf Marxen³, Peter J. Schmid⁴ and Taraneh Sayadi^{2,5}

¹ Department of Mathematics, Imperial College London, London, SW7 2AZ, United Kingdom.

² Institut Jean Le Rond d'Alembert, Sorbonne Université, CNRS, Paris, 75005, France.

³ Department of Mechanical Engineering Sciences, University of Surrey, Guildford, GU2 7XH, United Kingdom.

⁴ Department of Mechanical Engineering, King Abdullah University of Science and Technology, Thuwal, 23955, Saudi Arabia.

⁵ Institute of Combustion Technologies, RWTH-Aachen University, Aachen, 52062, Germany.

*Corresponding author(s). E-mail(s):
a.margaritis@imperial.ac.uk;

Abstract

In this paper, we present a methodology to achieve high-fidelity simulations of chemically reacting hypersonic flows and demonstrate our numerical solver's capabilities on a selection of configurations. The numerical tools are developed based on previous in-house codes for high-speed simulations with improvements in both numerical and physical modeling. Additionally, a modular, open-source library is coupled with the flow solver for modeling real-gas effects in variable atmospheric mixtures. Verification against literature is done for canonical flat-plate boundary layers with various choices for gas modeling, with excellent agreement observed in all cases. The implementation of an artificial-diffusivity shock-capturing numerical scheme is then verified for supersonic shockwave–boundary-layer interaction (SBLI)

cases and the improved code's capabilities are demonstrated for the cases of hypersonic SBLI and a sonic jet injection in a hypersonic crossflow, at higher enthalpy levels than those previously investigated. The results show excellent agreement with previous observations in the literature. The work presented in this paper demonstrates the range of applications that can be investigated with this tool, highlights the need for accurate physicochemical modeling, and paves the way for addressing increasingly more complex configurations and flows.

Keywords: hypersonics, boundary layers, reacting flow, chemistry, shockwave–boundary-layer interaction

1 Introduction

Recent advances in the aerospace sector have pushed the limits of vehicle design to far higher speeds and more extreme conditions than ever before. The revival of interest for complex orbital and inter-planetary missions, and the pursuit of commercial hypersonic flight, create the need for accurate and reliable atmospheric (re-)entry and hypersonic cruise vehicle design. Hypersonic boundary layers have posed a significant research and engineering challenge in this context, with fundamental research in hypersonic aerothermodynamics becoming a necessity [3, 37, 66, 75].

The flow environment encountered near the walls of a vehicle or object traveling at hypersonic speeds is an extremely complex problem, where the interfaces between disciplines become unclear. The interplay between thermodynamics, chemistry, and fluid mechanics creates an interdisciplinary problem that needs to be tackled by accounting for a variety of interconnected phenomena. Even in cases where each of these phenomena is well understood on its own, their combination is not always easy to model, predict, and interpret, as highlighted by a recent article [37] discussing these interactions for high-enthalpy high-speed flows; interactions which had already been recognized three decades earlier [24].

It is notoriously difficult and expensive to collect reliable experimental and in-flight data for hypersonic flows [67]. Due to the cost and difficulty of reliable experimental studies, accurate and reliable numerical simulations to characterize and predict the flow environment become even more indispensable. Typical numerical codes and tools fail to describe the complex and intricate nature of hypersonic flow, either due to unsuitable numerical techniques, or simply the lack of models for the multiphysical aspects of the flow.

The need for accurate and robust numerical simulations of hypersonic boundary layers has led researchers to the development of computational tools that solve the governing equations in the hypersonic flow regime. Initially focusing on the stability and transition of boundary layers, early investigations

have tried to extend concepts from subsonic and supersonic flow to the hypersonic regime for transition and instability evolution prediction [10, 38–40]. The recent work at the von Karman Institute for Fluid Dynamics (VKI) has provided thorough investigations of the effects of chemistry [49, 51–53, 78, 79, 81] and surface features, such as roughness, curvature [82, 83], and outgassing [50, 51, 54, 62], on the stability of boundary layers, using linear and nonlinear [49–54, 62, 78, 79, 81–83] stability analysis tools. An important outcome is the conflicting results these authors have sometimes found, which indicate, as they note, the immaturity of our understanding at this stage, concluding that incorrect modeling of transport phenomena could be as inaccurate as neglecting chemical activity altogether. Similar work has been conducted by the group of Candler using linear stability theory (LST) [25, 27] and parabolized stability equations (PSE) [26] for reacting flows, extending to shape optimization of hypersonic bodies [28, 58].

The thermal and chemical non-equilibrium (TCNEQ) effects are a significant modeling challenge in hypersonic flow simulations. At such high-energy gas states and given the extremely short time scales of hypersonic flows, there is no guarantee that collisions are frequent enough for energy exchange and chemical processes to reach equilibrium. Therefore, the composition and properties of the gases vary in space and time, following the relevant kinetics and thermodynamics. This creates the need for far more sophisticated gas models for the thermodynamic and transport properties of such gases. The significance of finite-rate phenomena is summarized in a recent comprehensive review [4]. In the continuum regime, the Navier-Stokes equations still hold for hypersonic reacting gases, with some necessary modifications for the gas properties and the addition of extra equations to model the chemical reactions and track the gas composition [29].

State-of-the-art tools for TCNEQ models have been developed to simulate the time evolution of the governing equations. A variety of powerful tools based on finite-volume techniques and multi-temperature (MT) models have been developed based on the work of Candler and MacCormack [5], leading to the numerical codes DPLR, using the data-parallel line relaxation (DPLR) method [80], and US3D [6, 7]. Such codes can be used for extracting the base flow for stability calculations or to simulate directly the nonlinear evolution of the flow [73, 74]. Such direct numerical simulation (DNS) results reveal the underlying prediction mechanisms of transition and serve as benchmarks for lower-fidelity prediction methods. More recent results have extended such simulations further into the turbulent regime [11–13, 59, 60, 68]. Other approaches have used high-order finite-difference large-eddy simulation (LES) and DNS solvers for such studies [18, 21, 42–48]. Initial efforts have been made to include real-gas effects and chemical non-equilibrium (CNEQ) modeling in the simulations by these authors.

The objective of this work is to develop a versatile computational tool that is able to accurately model hypersonic boundary layers including a number of phenomena involved in realistic problems, such as finite-rate chemistry effects

and shockwaves. For that, we extend a high-order finite-difference tool [56, 57] to include finite-rate chemistry modeling and shockwaves, building on previous work by Sayadi et al. [65] and Marxen et al. [48]. The real-gas and finite-rate chemistry effects are included by coupling our numerical tool with the Mutation++ library [69, 71], an open-source library developed by the VKI that is able to accurately calculate the thermodynamic, transport, and chemical kinetics properties of various high-enthalpy weakly-ionized gases. Verification of our computational tools is performed against previous results, while some new results are presented that showcase its capability to handle more complex cases. This novel computational tool is capable of including a multitude of physics that are very rarely dealt with simultaneously by numerical codes.

This paper is organized as follows. The fundamentals of hypersonic fluid dynamics are presented in Section 2, including the governing equations and basic modeling aspects. The numerical techniques employed are described in Section 3. Code verification and validation, and new results for more complex cases are discussed in Section 4. Finally, the main results are emphasized and conclusions are drawn in Section 5.

2 Background theory

In the following, we describe the general equations governing the flow problems discussed in this work. Our starting point is an overview of the conservation equations, followed by a detailed discussion of the various terms and modeling choices.

2.1 Governing conservation equations

The nondimensional Navier-Stokes equations for fluids that consist of a mixture of species, \mathcal{S} , are presented in Eqs. (1–4). Equation (1) is the continuity equation, describing the global mass conservation in the system. Equation (2) corresponds to the set of mass conservation equations for each species, with the net production rate terms, $\dot{\omega}_s$, appearing on the right-hand side. For non-reacting gas mixtures, where the mixture composition can be considered either constant or a direct function of the thermodynamic state, only the global mass conservation, Eq. (1), is needed; the species mass conservation equations, Eq. (2), are not necessary and can be omitted in this case. In order to ensure global mass conservation, in the case of a finite-rate reacting mixture with a varying composition, Eq. (1) needs to be solved together with Eq. (2) for all but one species. The omitted species is selected based on numerical considerations, commonly avoiding species with the smallest concentrations. Alternatively, all the species mass conservation equations can be solved while Eq. (1) is relaxed. For gases in thermal non-equilibrium (TNEQ), in which case different energy levels are treated independently, additional energy conservation equations are needed; these cases are not investigated in this work, since our attention is focused on cases where CNEQ effects are dominant.

$$\frac{\partial \rho}{\partial t} + \nabla \cdot (\rho \mathbf{u}) = 0 \quad (1)$$

$$\left\{ \frac{\partial \rho_s}{\partial t} + \nabla \cdot (\rho_s \mathbf{u} + \rho_s \mathbf{V}_s) = \dot{\omega}_s \right\}, \forall s \in \mathcal{S} \quad (2)$$

$$\frac{\partial \rho \mathbf{u}}{\partial t} + \nabla \cdot (\rho \mathbf{u} \otimes \mathbf{u}) = -\nabla p + \nabla \cdot \boldsymbol{\tau} \quad (3)$$

$$\frac{\partial \rho e_0}{\partial t} + \nabla \cdot (\rho h_0 \mathbf{u}) = \nabla \cdot (\boldsymbol{\tau} \cdot \mathbf{u}) - \nabla \cdot \mathbf{q} \quad (4)$$

The nondimensional quantities are time, t , density, ρ , velocity, \mathbf{u} , pressure, p , stress tensor, $\boldsymbol{\tau}$, total energy, e_0 , total enthalpy, h_0 , and heat flux, \mathbf{q} , along with the partial density, ρ_s , the net mass production rate, $\dot{\omega}_s$, and the diffusion velocity, \mathbf{V}_s , for species s . More details regarding the derivation of the equations and the validity of assumptions are provided in [1, 19, 29].

The governing equations, Eqs. (1–4), can be brought into the following compact form, seen in Eqs. (5) and (6).

$$\frac{\partial \mathbf{Q}}{\partial t} = -\nabla \cdot \mathbf{F}_C + \nabla \cdot \mathbf{F}_D + \mathbf{S} = \mathbf{F}(\mathbf{Q}) \quad (5)$$

$$\mathbf{Q} = \begin{bmatrix} \rho \\ \rho_{s_1} \\ \vdots \\ \rho_{s_{N_s}} \\ \rho \mathbf{u} \\ \rho e_0 \end{bmatrix}, \mathbf{F}_C = \begin{bmatrix} \rho \mathbf{u} \\ \rho_{s_1} \mathbf{u} \\ \vdots \\ \rho_{s_{N_s}} \mathbf{u} \\ \rho \mathbf{u} \otimes \mathbf{u} + p \\ \rho h_0 \mathbf{u} \end{bmatrix}, \mathbf{F}_D = \begin{bmatrix} 0 \\ -\rho_{s_1} \mathbf{V}_{s_1} \\ \vdots \\ -\rho_{s_{N_s}} \mathbf{V}_{s_{N_s}} \\ \boldsymbol{\tau} \\ \boldsymbol{\tau} \cdot \mathbf{u} - \mathbf{q} \end{bmatrix}, \mathbf{S} = \begin{bmatrix} 0 \\ \dot{\omega}_{s_1} \\ \vdots \\ \dot{\omega}_{s_{N_s}} \\ 0 \\ 0 \end{bmatrix} \quad (6)$$

As mentioned above, there are N_s conservation equations for the species, so the total problem involves $N_s + 5$ equations. However, only $N_s - 1$ of the N_s species conservation equations need to be solved. Therefore, the final problem involves $N_s + 4$ scalar equations.

The nondimensionalization of the equations is done with the reference parameters in Eq. (7), where $\tilde{T}_{\text{ref}} = (\tilde{\gamma}_\infty - 1)\tilde{T}_\infty$ and the speed of sound is c .

$$\rho = \frac{\tilde{\rho}}{\tilde{\rho}_\infty}, p = \frac{\tilde{p}}{\tilde{\rho}_\infty \tilde{c}_\infty^2}, T = \frac{\tilde{T}}{\tilde{T}_{\text{ref}}}, \mathbf{u} = \frac{\tilde{\mathbf{u}}}{\tilde{c}_\infty}, \rho_s = \frac{\tilde{\rho}_s}{\tilde{\rho}_\infty}, \mathbf{V}_s = \frac{\tilde{\mathbf{V}}_s}{\tilde{c}_\infty} \quad (7)$$

$$k = \frac{\tilde{k}}{\tilde{k}_\infty}, \mu = \frac{\tilde{\mu}}{\tilde{\mu}_\infty}, e_0 = \frac{\tilde{e}_0}{\tilde{c}_\infty^2}, h_0 = \frac{\tilde{h}_0}{\tilde{c}_\infty^2}, \dot{\omega}_s = \frac{\tilde{\dot{\omega}}_s}{\tilde{\rho}_\infty \tilde{c}_\infty / \tilde{L}_{\text{ref}}}$$

The definitions in Eq. (8) are used for the nondimensional total energy, e_0 , internal enthalpy, h , and total enthalpy, h_0 , respectively.

$$e_0 = \frac{e}{Ec} + \frac{1}{2} \|\mathbf{u}\|^2, \quad h = e + \frac{p}{\rho}, \quad h_0 = e_0 + \frac{p}{\rho}, \quad (8)$$

where the nondimensional internal energy is denoted e . The stress tensor, $\boldsymbol{\tau}$, and heat flux, \mathbf{q} , are computed as in Eqs. (9) and (10), respectively.

$$\boldsymbol{\tau} = \frac{\mu}{Re_\infty} \left(\nabla \mathbf{u} + (\nabla \mathbf{u})^T - (\nabla \cdot \mathbf{u}) \mathbf{I} \right) \quad (9)$$

$$\mathbf{q} = -\frac{k}{Re_\infty Pr_\infty Ec_\infty} \nabla T + \sum_{s \in \mathcal{S}} \rho_s h_s \mathbf{V}_s \quad (10)$$

The second term on the right-hand side of equation Eq. (10) is included only in the case of finite-rate chemistry (see Section 2.2.1.1). The nondimensional Reynolds number, Re_∞ , and Prandtl number, Pr_∞ , are defined in the free stream at the domain inlet. The Eckert number, Ec_∞ , is also computed at the free stream and is equal to one by design. These nondimensional quantities are defined as

$$Re_\infty = \frac{\tilde{\rho}_\infty \tilde{c}_\infty \tilde{L}_{\text{ref}}}{\tilde{\mu}_\infty}, \quad Pr_\infty = \frac{\tilde{\mu}_\infty \tilde{c}_{p_\infty}}{\tilde{k}_\infty}, \quad Ec_\infty = \frac{\tilde{c}_\infty^2}{\tilde{c}_{p_\infty} \tilde{T}_{\text{ref}}}. \quad (11)$$

The thermodynamic properties and equation of state, as well as the transport properties and the chemical kinetics terms depend on the modeling choices and are discussed in detail in the following Section 2.2.

2.2 Thermodynamic and chemical models

A variety of models with different levels of complexity are implemented in the solver used in this work. In the following, we discuss the details of each modeling approach and the implications of the underlying assumptions on the closure of the governing equations.

2.2.1 Multi-component gas mixtures with variable composition

In the general case, a reacting gas in a high-enthalpy flow is considered a multi-component mixture that consists of a set of species \mathcal{S} , interacting via a defined network of reactions, as seen in Section 2.2.1.1. The variation of the species fractions makes the chemical reaction and diffusion terms in the governing equations significant, hence they need to be modeled using various assumptions.

For a multi-component gas mixture, the global mixture properties are derived from the species properties based on,

$$\rho = \sum_{s \in \mathcal{S}} \rho_s, \quad e = \sum_{s \in \mathcal{S}} Y_s e_s, \quad h = \sum_{s \in \mathcal{S}} Y_s h_s, \quad (12)$$

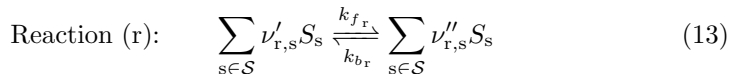
where the species mass fraction is $Y_s = \frac{\rho_s}{\rho}$, with $\sum_{s \in \mathcal{S}} Y_s = 1$. The mixture's thermodynamic and transport properties depend, in general, on any two thermodynamic properties, for example the temperature and the pressure, which define the thermodynamic state of the mixture, and on its composition. The composition is generally an independent variable. It can potentially become dependent on other thermodynamic quantities for the special cases seen in Section 2.2.1.2.

The individual species properties are accurately computed using kinetic theory and statistical mechanics [69, 70]. The thermochemical library Mutation++ [71] is used to compute thermodynamic and transport properties at different conditions.

2.2.1.1 Finite-rate chemistry and CNEQ

When finite-rate chemistry cannot be neglected, the species mass production rate, $\dot{\omega}_s$, and the species diffusion velocities, \mathbf{V}_s , need to be modeled. These terms are described in this section.

In a general case, a set of reactions, \mathcal{R} , is considered depending on the mixture in question. Each reaction, r is characterized by a reaction rate, R_r , which is computed by the forward rate, k_{f_r} , and the backward rate, k_{b_r} . These, in turn, are obtained according to experimentally or theoretically calibrated Arrhenius formulas in the form $k_{f_r} = C_r T^{n_r} \exp(T_{a_r}/T)$, and $k_{b_r} = k_{f_r}/K_{\text{eq}_r}(T)$, where K_{eq_r} is the reaction equilibrium constant at specific conditions. This description is given in Eq. (13) for a generic reaction.



The net reaction rate is then given by

$$R_r = \left[k_{f_r} \Pi_s \left(\frac{\rho_s}{M_s} \right)^{\nu'_{r,s}} - k_{b_r} \Pi_i \left(\frac{\rho_s}{M_s} \right)^{\nu''_{r,s}} \right] \cdot \sum_{s \in \mathcal{S}} \left(Z_{r,s} \frac{\rho_s}{M_s} \right), \quad (14)$$

where the species molar mass is M_s and the efficiency of species s as a third-body in reaction r is $Z_{r,s}$. The net mass production rates for species s from all reactions are obtained as

$$\dot{\omega}_s = M_s \sum_{r \in \mathcal{R}} (\nu''_{r,s} - \nu'_{r,s}) R_r. \quad (15)$$

The reader is referred to the description provided in [69, 71], on which the Mutation++ library is based, for further details.

The diffusion flux, $\mathbf{J}_s = \rho_s \mathbf{V}_s$ appearing in Eq. (2) also needs to be modeled in this case. Following the description in [46], and under the same assumptions, neglecting thermal and barodiffusion, the diffusion driving force for each

species, \mathbf{d}_s , reduces to its molar fraction gradient,

$$\mathbf{d}_s = \nabla X_s. \quad (16)$$

In the general case, the diffusion velocity for each species s , \mathbf{V}_s , is then the solution of the Stefan-Maxwell linear system of equations for a multi-component mixture,

$$\left\{ \sum_{i \in \mathcal{S}} Q_{s,i} \mathbf{V}_i = -\mathbf{d}_s \right\}, \quad \forall s \in \mathcal{S} \quad (17)$$

where, $Q_{s,i}$ is the Stefan-Maxwell interaction coefficient for the pair of species s and i .

While solving the system in Eq. (17) is the most accurate way to calculate the diffusion fluxes in a multi-component gas mixture, simpler formulations are found in the literature under the same assumptions [15, 63]. A simpler expression based on Fick's diffusion model (applicable to binary mixtures) with a mass correction is given below in Eq. (18),

$$\mathbf{J}_s = -cM_s D_s \nabla Y_s + cY_s \sum_{i \in \mathcal{S}} M_i D_i \nabla Y_i. \quad (18)$$

Here, $c = \sum_{s \in \mathcal{S}} (\rho_s / M_s)$ and D_s is the averaged diffusion coefficient for species s , defined as

$$D_s = \frac{1 - X_s}{\sum_{r \neq s} X_r / D_{s,r}}. \quad (19)$$

In lieu of solving a linear system of equations of size N_s , using this model, the diffusion flux is computed from an algebraic equation, at a significantly reduced computational cost. Both implementations are available in the solver presented here, and the accuracy of the simplified approach is verified for practical cases. The constraints seen in Eq. (20) have to be respected for the kinetic and diffusive terms, hence

$$\sum_{s \in \mathcal{S}} \dot{\omega}_s = 0, \quad \sum_{s \in \mathcal{S}} \rho_s \mathbf{V}_s = 0. \quad (20)$$

The heat flux takes the original form shown in Eq. (10), where the thermal conductivity is replaced by its frozen composition value. The diffusive heat flux is then taken into account explicitly through the second term in that definition. The remaining relevant thermodynamic and transport properties are given by general relations that are implemented in the Mutation++ library.

2.2.1.2 *Special cases: frozen and equilibrium flow*

There exist two extreme cases for a multi-component mixture, where its composition becomes irrelevant.

- **Frozen composition**, when the reaction time scale is too long compared to the flow time scale, hence the composition of the flow is generally constant in time.

- **Local thermodynamic equilibrium (LTE)**, when the reaction time scale is short enough for the reactions to bring the mixture to a state of local equilibrium, where the composition is identical to its equilibrium composition that can be computed from thermodynamic relations by maximizing the system entropy or, equivalently, minimizing the Gibbs free energy.

In both cases of frozen composition and local thermodynamic equilibrium (LTE), the mixture composition becomes a dependent variable, directly computed for a given thermodynamic state. Therefore, the species mass conservation equations, Eq. (2), and the corresponding reaction and diffusion terms are not needed. The heat flux takes the simplified form shown in Eq. (21),

$$\mathbf{q} = -\frac{k}{Re_\infty Pr_\infty Ec_\infty} \nabla T, \quad (21)$$

where the thermal conductivity is computed at either frozen or LTE conditions. In the latter case, the diffusive effect at equilibrium is included in its value.

In situations between these extremes, finite-rate chemistry needs to be tracked as described in Section 2.2.1.1 and the mixture composition changes in space and time.

2.2.2 Calorically and thermally perfect gases

When the gas is assumed to be calorically or thermally perfect, the composition becomes irrelevant. The chemical diffusion and reaction terms in the governing equations vanish, and the thermodynamics and transport properties become simple functions of the thermodynamic state of the gas, resulting in a nondimensional equation of state given by

$$p = \rho \frac{\gamma - 1}{\gamma Ec_\infty} T. \quad (22)$$

It should be noted that this formulation is valid in this form only for the calorically perfect gas (CPG) and thermally perfect gas (TPG) models. In the case of reacting mixtures with variable composition, the right hand side needs to be scaled by a factor accounting for the change of gas constant and depends on the composition.

In the case of a CPG, the thermodynamic properties, such as the specific heat, are considered constant. The internal energy and enthalpy thus become linear functions of temperature, in nondimensional form $\gamma_\infty e = T$, which is derived from the dimensional form $\tilde{h} = \tilde{c}_{p_\infty} \tilde{T}$. Nondimensionally, $k = \mu$.

In the case of a TPG, the thermodynamic properties are generally functions of temperature. Since the specific heat is now itself a function of temperature, the internal energy and enthalpy become nonlinear functions of temperature. The relations used are based on the work presented in [39, 45]. The specific

heat is given as

$$\tilde{c}_p(\tilde{T}) = \tilde{c}_p^0 \left(1 + \frac{\tilde{\gamma}_\infty - 1}{\tilde{\gamma}_\infty} \left(\frac{\tilde{\Theta}}{\tilde{T}} \right)^2 \frac{e^{\tilde{\Theta}/\tilde{T}}}{e^{\tilde{\Theta}/\tilde{T}} - 1} \right), \quad (23)$$

where $\tilde{\Theta} = 3055 \text{ K}$ and \tilde{c}_p^0 such that $\tilde{c}_p(\tilde{T}_\infty) = \tilde{c}_{p\infty}$. The transport properties (viscosity and thermal conductivity) can be constant or follow analytical expressions as functions of temperature.

In both the CPG and TPG assumptions, the viscosity is computed using Sutherland's law,

$$\tilde{\mu}(\tilde{T}) = \tilde{C}_1 \frac{\tilde{T}^{3/2}}{\tilde{T} + \tilde{T}_S}, \quad (24)$$

where $\tilde{C}_1 = 1.458 \times 10^{-6} \text{ kgm}^{-1}\text{s}^{-1}\text{K}^{-1/2}$ and $\tilde{T}_S = 110.4 \text{ K}$.

In addition, in both cases the heat flux takes the simplified form seen in Eq. (21) as the diffusive heat flux vanishes. In CPG, the equilibrium conductivity is assumed constant, $\tilde{k} = \tilde{k}_\infty$, while k can be computed as in Eq. (7). Whereas, in TPG, the equilibrium thermal conductivity is approximated by Keyes' law,

$$\tilde{k}(\tilde{T}) = \tilde{C}_2 \frac{\tilde{T}^{1/2}}{1 + \left(\tilde{C}_3/\tilde{T} \right) 10^{-\tilde{C}_4/\tilde{T}}}, \quad (25)$$

with $\tilde{C}_2 = 2.646 \times 10^{-3} \text{ Wm}^{-1}\text{K}^{-3/2}$, $\tilde{C}_3 = 245.4 \text{ K}$, $\tilde{C}_4 = 12 \text{ K}$.

3 Numerical framework

The following section outlines the numerical framework of the Navier-Stokes solver and the implementation of the models described so far.

3.1 Discretization in space and time

The computational tools developed are based on the original Navier-Stokes solver developed by Nagarajan [56, 57]. The code has been applied to DNS and LES studies of flat-plate boundary layers in the subsonic [65] and the supersonic [45–48] regime.

Space discretization is done using fourth-order or sixth-order compact finite differences [36]. The governing equations are formulated in curvilinear coordinates and solved on a staggered grid, as seen in Fig. 1. A detailed discussion of the curvilinear transformation is found in [56].

Time discretization is done using explicit third-order or fourth-order Runge-Kutta schemes. Specifically, the low-memory two-register RK3 scheme, the three-register total variation diminishing (TVD) RK3 and RK4 [8, 35] are implemented.

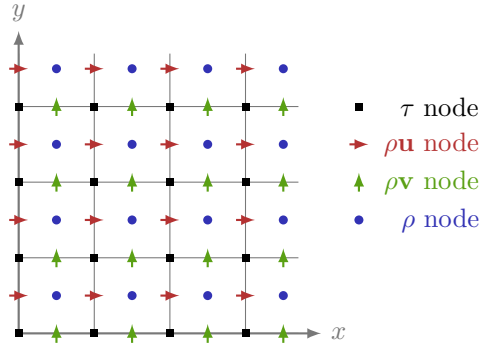


Fig. 1: Schematic of a staggered grid in two dimensions. The cell-centered ρ nodes are where scalar variables are stored and computed, while the interface nodes ρu and ρv are where the streamwise and wall-normal velocities, fluxes, and gradients are stored and computed. The τ nodes are the grid nodes where the grid is generated, and where the solution is interpolated for post-processing and presentation. Extension to three dimensions is trivial, with an additional ρw node at the interface in the page-normal direction, for the spanwise velocities, fluxes, and gradients.

3.2 Boundary conditions

A general sketch of the domain of interest is presented in Fig. 2. A reference solution (typically, a self-similar boundary layer) is prescribed in the sponge regions, and the time-advanced solution is forced towards that reference by incorporating damping source terms in the right-hand side of the equations, as seen in Eq. (26).

$$\frac{\partial \mathbf{Q}}{\partial t} = \mathbf{F}(\mathbf{Q}) - \sigma(\mathbf{x})(\mathbf{Q} - \mathbf{Q}_{\text{ref}}) \quad (26)$$

The sponge parameter $\sigma(\mathbf{x})$ is a smooth third-order polynomial function of space, vanishing inside the domain and reaching a high value near the boundaries which is selected empirically. The sponge can be completely omitted at the inflow in cases where it is not necessary, such as hypersonic flow where upstream-traveling disturbances are minimal. Flow perturbations are also forced to vanish inside the sponge regions. The wall boundary is either adiabatic or isothermal, while no slip and no catalysis is permitted for the reacting cases. Other boundary conditions, such as blowing and suction at the wall, isolated roughness geometries, or jet injections, are also implemented and available.

3.3 Shock-capturing scheme

In the presence of shocks and discontinuities special treatment is necessary. Out of the variety of approaches that exist, we opted for a numerical scheme based

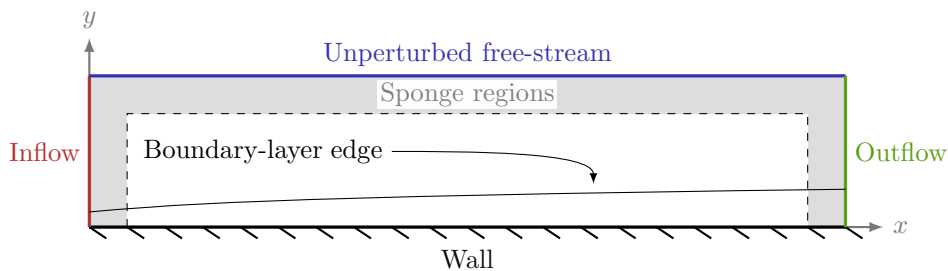


Fig. 2: Schematic of a generic computational domain. Inflow and outflow can be enforced with reference solutions. The same approach is used at the free-stream. The wall is non-catalytic, either isothermal or adiabatic. A variety of forced boundary conditions can be applied locally on the wall.

on artificial molecular and bulk viscosity. This scheme has previously been implemented and verified for shock capturing in hypersonic flow simulations. Further details can be found in [16, 32, 34, 41].

3.4 Coupling with the Mutation++ library

The thermodynamic and transport properties, and the source terms for chemical kinetics models, are extracted from the Mutation++ library [71]. The library, written in C++, is coupled with the solver, written in Fortran 95, using a wrapper interface that facilitates the library function calls by implementing them as functions and subroutines in the solver. An on-the-fly communication between the solver and the library is necessary, with constant evaluation of the thermochemical and transport properties at each grid point, given the local state vector. Quantities are therefore exchanged between the solver and the library for each grid point, at each time step. These function evaluation calls add a significant computational overhead to the solver, since each state evaluation involves the iterative solution of nonlinear equations. Concepts and techniques that would accelerate these evaluations are investigated as part of ongoing work. The library offers valuable modularity, decoupling the thermochemical model from the core of the solver, and offering multiple capabilities to change gas mixtures, databases, and models.

3.4.1 Comparison between perfect-gas and real-gas models

Benchmark simulations have been run to compare the accuracy and computational cost of the various thermochemical models implemented in the solver. The flexibility and extended validity of the use of Mutation++ comes with a large computational cost. The total simulation time is increased by more than one order of magnitude when using the CNEQ model compared to the CPG model, and by a factor of about five compared to the TPG model. A reduction

of about 40% in computational cost can be achieved using an algebraic diffusion model, as discussed in Section 2.2.1.1, compared to the Stefan-Maxwell diffusion model, with minimal impact on the accuracy for the cases investigated in this work.

4 Results

In this section, a set of cases are investigated in order to verify the methodology presented so far and to investigate the effect of gas model selection on the resulting flow in different configurations. These cases include adiabatic and isothermal $Ma = 10$ laminar boundary layers, forced with Tollmien-Schlichting waves (see Table 1), laminar shockwave-boundary-layer interaction (SBLI) at $Ma = 2$ and $Ma = 5.92$, and a jet in hypersonic crossflow at $Ma = 5$.

4.1 Hypersonic flat-plate boundary layers

A set of two hypersonic boundary layers in Earth's atmosphere at $Ma = 10$, based on Marxen et al. [46, 48], are considered here to verify the implementation of the numerical method presented in Section 3. First, the steady state solution and then the growth rate of forced Tollmien-Schlichting instabilities inside the two-dimensional boundary layer are compared. The main configurations considered are: (i) case I (isothermal), and (ii) case A (adiabatic), referring to the boundary condition imposed on the wall. The setup parameters and freestream conditions for both cases are presented in Table 1, where ω and A are related to the forced perturbation and explained in Section 4.1.1.

	Isothermal Case (I)	Adiabatic Case (A)
Ma_∞	10.0	
Re_∞	10^5	
$T_\infty [K]$	278	350
$\tilde{p}_\infty [Pa]$	4135	3596
T_{wall}/T_∞	4.31	-
ω	45	34
A/Ma_∞	10^{-3}	

Table 1: Thermodynamic and freestream conditions for the $Ma = 10$ hypersonic boundary layers investigated in this study (adapted from [46]).

The computational domain considered here has a finer resolution than in the previous studies. The nondimensional grid size in the streamwise direction is $\Delta x = 0.075$, simulating a domain from $x_0 = 14.0$ to $x_1 = 86.0$ using 960 grid points. The sponge regions extend for 5 and 15 nondimensional units at the inflow and outflow, respectively. In the wall-normal direction, 211 grid points are used, clustered near the wall using Eq. (27), with the last 26 points in the free stream used in the sponge region. Table 2 summarizes the details of the computational domain as well as the resulting resolution.

$$y(m) = y_0 + (y_1 - y_0) \left((1 - \kappa_y) \left(\frac{m-1}{NY-1} \right)^3 + \kappa_y \left(\frac{m-1}{NY-1} \right) \right), \quad m \in [1, NY] \quad (27)$$

Case	x_0	x_1	y_0	y_1	κ_x	κ_y	N_x	N_y
Case A	14.0	86.0	0	1.6	1.0	0.15	960	211
Case I	14.0	86.0	0	1.6	1.0	0.15	960	211

Table 2: Mesh configuration for the hypersonic boundary layer simulations

All three thermochemical models are systematically tested on both cases. The CNEQ model uses a 5-component air mixture composed of N₂, O₂, N, O, and NO.

4.1.1 Disturbance forcing

Tollmien-Schlichting waves are harmonically forced on the converged steady-state solution of the unforced equations using blowing and suction on a strip extending from $x = 19.3$ to $x = 20.7$. For case A, the wall condition is switched to isothermal for the perturbations, assuming only small deviations from the steady-state temperature. The disturbance has a nondimensional forcing frequency ω given in Eq. (28).

$$\omega = F Ma_\infty^2 Re_\infty, \quad \text{with} \quad F = 2\pi \tilde{f} \frac{\tilde{\mu}_\infty}{\tilde{\rho}_\infty \tilde{u}_\infty^2} \quad (28)$$

Here \tilde{f} is the dimensional frequency of the disturbance. The forcing amplitude is small enough to ensure that the disturbance evolution is linear, i.e. $A = 10^{-3} Ma_\infty$.

The simulation is advanced until transient effects are advected out of the domain and a time-periodic state is achieved. Flow snapshots are collected over two forcing periods and the Fourier transformation is applied, giving a complex Fourier coefficient $\hat{\phi}_j$ for a given harmonic j and a given quantity $\phi \in [\rho, u, v, w, T, \dots]$. Only the results for the first harmonic are presented in Section 4.1.2 and Section 4.1.3. The streamwise disturbance amplification is computed using the wall-normal maxima of the amplitudes of the disturbance quantity $\hat{\phi}_1$,

$$\hat{\phi}_1^{max}(x) = \max_y (|\hat{\phi}_1(x, y)|) \quad (29)$$

and the normalized growth rate $\alpha_{i,1}$ is computed as follows, for example for the wall-normal velocity, i.e for $\phi = v$, it is

$$\alpha_{i,1}(x) = \frac{1}{\hat{v}_1^{max}} \frac{\partial \hat{v}_1^{max}}{\partial x} \frac{Re_x}{Re_\infty}. \quad (30)$$

In all the above, sponge regions are not considered in the calculations. In the following analysis, the streamwise varying Reynolds number is defined as $Re_x = \sqrt{x Re_\infty Ma_\infty}$.

4.1.2 Isothermal wall – Case I

The mean streamwise velocity and temperature profiles at a streamwise Reynolds number location $Re_x = 2000$ for case I are presented in Fig. 3, compared with the results of Marxen et al. [46], where only the TPG model was investigated. This figure shows both TPG profiles to be in perfect agreement as expected. In addition, both the LTE and CNEQ models show only minor differences compared to the TPG solution. This is expected as the isothermal condition induces a maximum temperature of $T_{\max} \approx 1740K$ in the boundary layer. Below 2000K air chemistry is known to be mostly irrelevant [1] with almost negligible dissociation. Hence, the thermally perfect gas assumption holds reasonably well, resulting in similar behavior regardless of the model selected.

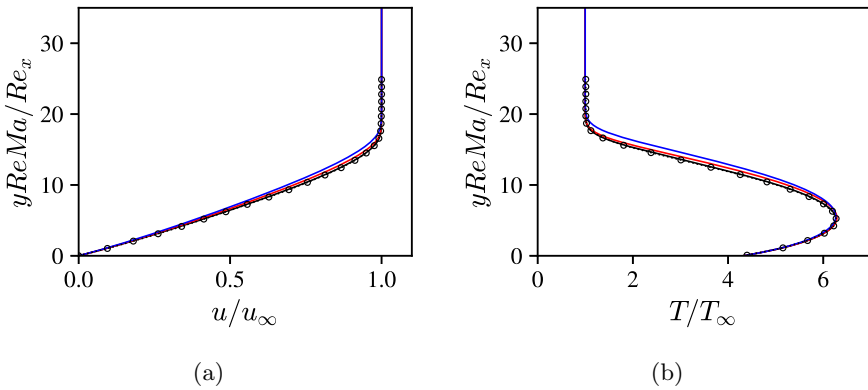


Fig. 3: (a) Streamwise velocity, u , and (b) temperature, T , profiles in the boundary layer for case I at $Re_x = 2000$. Current results (solid lines) are compared to Marxen et al. [46] (dotted lines with symbols) for different gas models: TPG (black), LTE (blue), CNEQ (red).

In Fig. 4 we see the baseflow solution for the streamwise velocity, in Fig. 4a, and a snapshot of the evolution of the forced perturbation, in Fig. 4b. Finally, Fig. 4c shows the growth rate α_i of the Tollmien-Schlichting waves in this case. While some differences are observed upstream, perfect agreement is found downstream with the results of Marxen et al. [46] for the TPG model. The current simulations are better resolved than those of Marxen et al. [46], and the improved resolution has been found to explain the more accurate prediction and the disappearance of small oscillations upstream. Interestingly, despite the

CNEQ baseflow being almost identical to that of the TPG model, the instability grows earlier in the boundary layer and to a higher amplitude compared to the case modeled using a TPG assumption. Thus, finite-rate chemistry alters the growth and decay of the perturbations directly, even though it has a negligible effect in the baseflow solution, potentially altering the stability and transition behavior without an obvious effect on the baseflow.

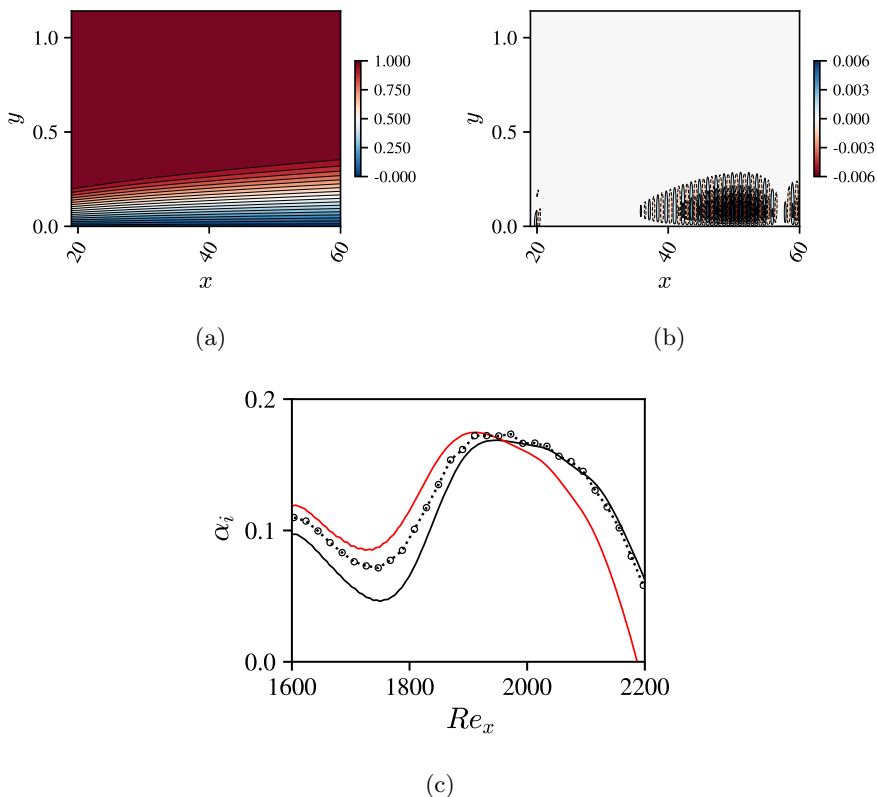


Fig. 4: (a) Mean streamwise velocity field, u , and (b) wall-normal perturbation velocity field, v' , for case I. (c) Streamwise growth rate, α_i , of the linear perturbation in the isothermal boundary layer with respect to Re_x . Current results (solid lines) are compared to Marxen et al. [46] (dotted lines with symbols) for different gas models: TPG (black), CNEQ (red).

4.1.3 Adiabatic wall – Case A

In the adiabatic case, a higher freestream temperature is imposed by design to promote CNEQ effects.

The mean flow and temperature profiles at a streamwise Reynolds number location $Re_x = 2000$ are presented in Fig. 5 and compared to the results of Marxen et al. [46]. Similar to the isothermal case, practically perfect agreement is found for all models compared to the previous results. However, in this case the baseflows differ significantly depending on the model used for the gas. Wall temperature decreases significantly from a frozen-chemistry (fixed-composition) assumption to a CNEQ model to an LTE model. These results indicate that the CNEQ effects in the flow are significant in this case and need to be accounted for to achieve accurate baseflow predictions.

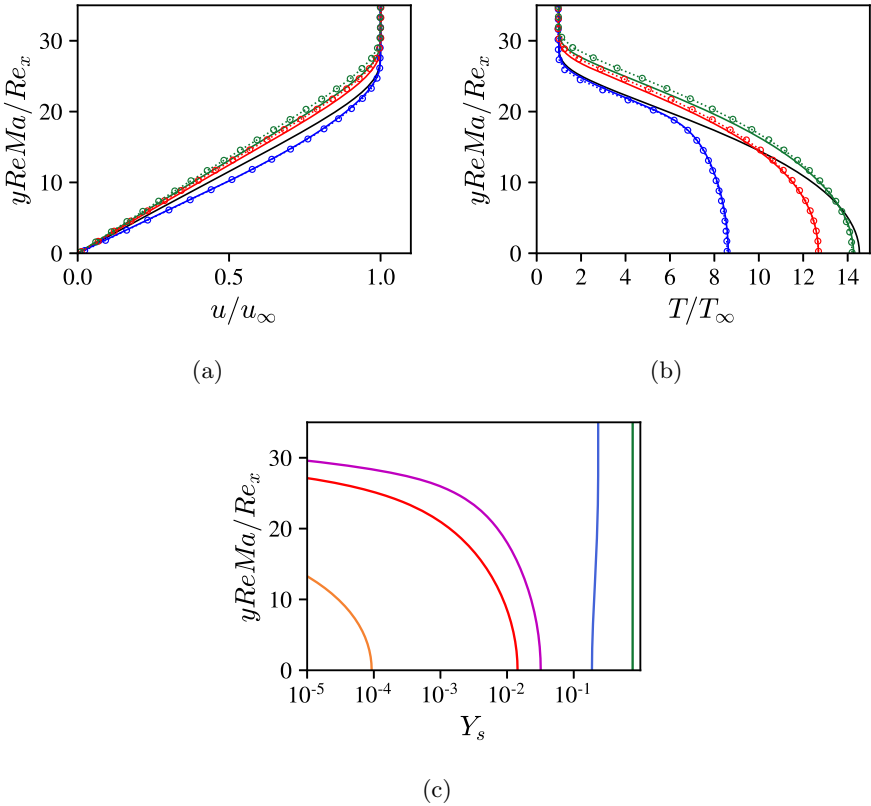


Fig. 5: (a) Streamwise velocity, u , and (b) temperature, T , profiles in the boundary layer for case A at $Re_x = 2000$. Current results (solid lines) are compared to Marxen et al. [46] (dotted lines with symbols) for different gas models: TPG (black), LTE (blue), CNEQ (red), frozen chemistry (green). (c) Species mass fractions at $Re_x = 2000$. From left to right : N , NO , O , O_2 , N_2 .

Due to the near-wall temperature approaching $T_{\text{wall}} \approx 4900\text{K}$ near the inflow, N_2 and O_2 rapidly start to dissociate to N , O , NO through endothermic chemical reactions. This is illustrated in Fig. 5c, presenting all the mass fraction profiles at the streamwise location where $Re_x = 2000$. Close to the wall, O_2 mass fraction decreases while O and NO are produced. To a smaller extent, N is also created through N_2 dissociation. Moreover, the dissociated species concentrations (O , NO , N) build up as the species are also convected downstream while continuously being produced. Consequently, the wall temperature decreases progressively along the streamwise direction due to cooling by endothermic dissociation.

In Fig. 6 we see the baseflow solution for the streamwise velocity, in Fig. 6a, and a snapshot of the evolution of the forced perturbation, in Fig. 6b. Figure 6c shows the corresponding growth-rates in the adiabatic case. Correct agreement is found for the CNEQ model up to $Re_x = 1950$. Downstream, the computed growth rate differs slightly from the previous results but the overall trend is similar. This difference is explained by the evolution of the thermodynamic and kinetics models used in the corresponding libraries. The growth rate in the TPG model is however noticeably different compared to the cases using the CNEQ model, highlighting the inadequacy of such models in high-enthalpy cases.

In order to confirm the reduction in CPU time using Ramshaw's simplified algebraic diffusion model (see Section 2.2.1.1), with negligible impact on the accuracy of the results, the base flow and growth rates of Tollmien-Schlichting waves for case A are computed using equation Eq. (18). Base flows are practically identical in terms of all relevant variables. Similarly, as shown in Fig. 6c, the growth rate is in almost perfect agreement with that computed using the Stefan-Maxwell model. A slight discrepancy is observed, which can be attributed to small changes in the diffusion fluxes. Therefore, Eq. (18) is a good compromise between performance and physical accuracy. The same model was also used in various numerical studies of hypersonic boundary layer with finite-rate chemistry [11–13, 59].

4.2 2D shockwave–boundary-layer interaction

Supersonic and hypersonic flows over complex geometries usually present SBLI. The large pressure gradient induced by the impinging shock may cause separation of the boundary layer with the occurrence of a recirculation bubble. This bubble can in turn change the stability characteristics of the flow on the vehicle surface. In the following section, we first validate the capability of the code to accurately simulate SBLI against a benchmark shockwave laminar boundary layer experiment. Then, a higher Mach number case is designed, based on [23], with a high freestream temperature, to directly assess the effect of finite-rate chemistry compared to a perfect gas assumption.

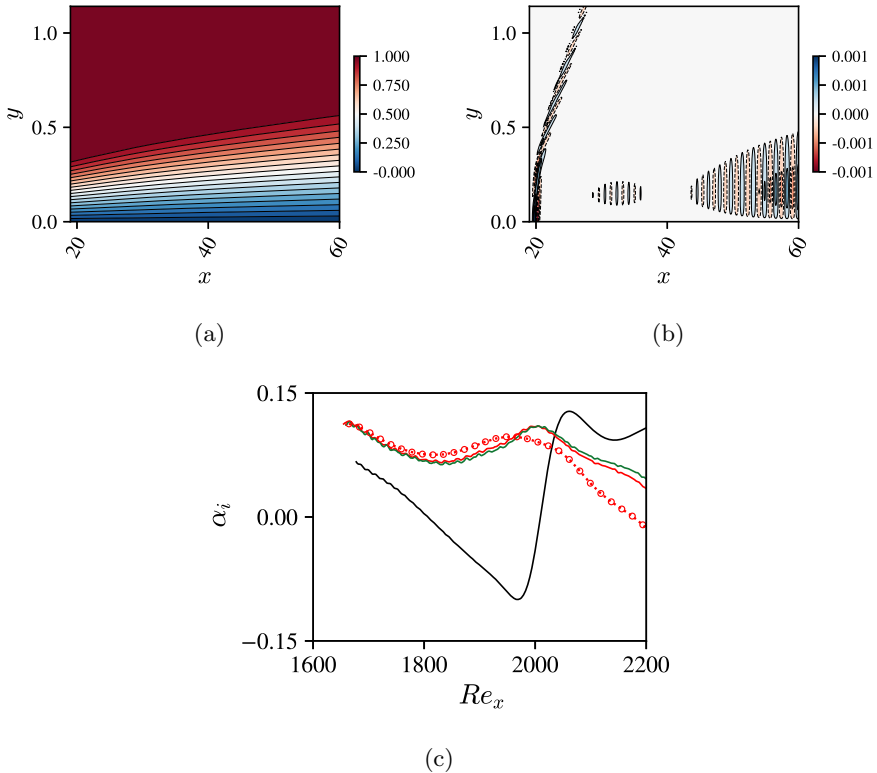


Fig. 6: (a) Mean streamwise velocity field, u , and (b) wall-normal perturbation velocity field, v' , for case A. (c) Streamwise growth rate, α_i , of the linear perturbation in the adiabatic boundary layer with respect to Re_x . Current results (solid lines) are compared to Marxen et al. [46] (dotted lines with symbols) for different gas models: TPG (black), CNEQ with the Stefan-Maxwell multi-component diffusion model (red), CNEQ with Ramshaw's simplified diffusion model (green).

SBLI Case	$x_0 - x_1$	$y_0 - y_1$	κ_x	κ_y	N_x	N_y
$Ma_\infty = 2.0$	0.30 – 1.55	0.0 – 0.35	1.0	0.15	960	501
$Ma_\infty = 5.92$	19.0 – 254.0	0.0 – 36.0	1.0	0.15	960	450

Table 3: Mesh configuration for the two SBLI cases investigated.

4.2.1 2D SBLI at $Ma = 2$

The capability of the solver to correctly simulate compressible flows including shocks is verified using a benchmark SBLI case, first investigated experimentally by Hakkinen et al. [22] and later numerically in several studies [31, 55]. In this case, a laminar $Ma_\infty = 2$ boundary layer over an adiabatic plate is

separated by an impinging shock with a shock angle of $\theta \approx 32^\circ$. The Reynolds number based on the impinging location of the shock is $Re_{x_0} = 3 \cdot 10^5$. All other flow conditions match the simulation by Katzer [31]. In the top-sponge opposite of the wall, Rankine-Hugoniot oblique shock relations are used to propagate the oblique shock downward, progressively introducing the discontinuity into the domain.

The grid used in that case is finer than in the previous studies, using respectively 960 and 501 points in the streamwise and wall-normal directions. All grid parameters are specified in Table 3.

Figure 7 shows the density field after convergence of the residuals to machine-precision. All relevant flow features of the SBLI are present: the recirculation bubble, the separation shock, the expansion fan, and the reflected shock. The results compare well to those of [55]. Figure 8 presents the skin friction coefficient and wall pressure along the wall. These match previous results almost perfectly.

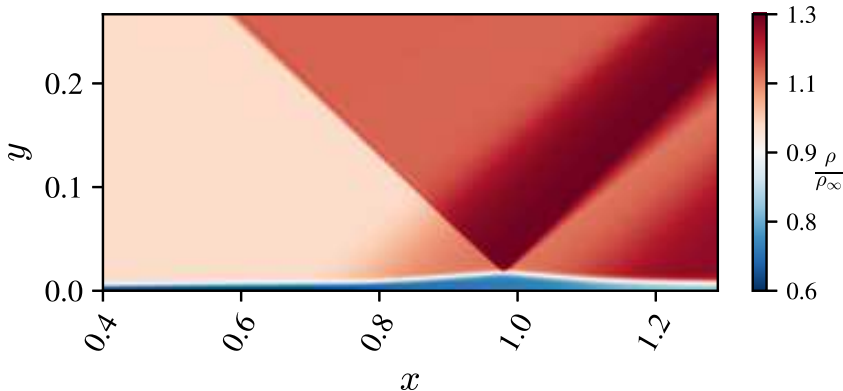


Fig. 7: Density contour for the $Ma_\infty = 2$ laminar SBLI case. The impinging and reflected shockwaves are visible, as well as the recirculation bubble and other relevant flow features.

4.2.2 2D SBLI at $Ma = 5.92$

Furumoto et al. [17] studied the real-gas effects on a steady oblique SBLI at $Ma = 7$. The high enthalpy at the freestream leads to Oxygen and Nitrogen dissociation and reduction of the size of the recirculation region as well as peak heating on the surface due to the endothermic real-gas effects. However, Furumoto et al. note that the thermochemical model used was rather simplistic. More recently, Volpiani [77] studied an oblique SBLI at $Ma = 6$ in chemical non-equilibrium with both laminar and turbulent inflow boundary layers. These results highlight the same trend, with a smaller recirculation bubble

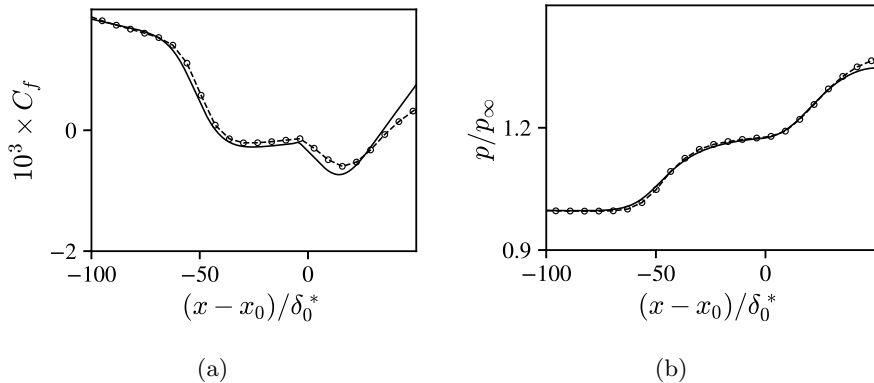


Fig. 8: Verification of the $Ma_\infty = 2$ laminar SBLI case against literature. (a) Skin friction coefficient and (b) normalized wall pressure streamwise distributions. The impinging shock location is marked with x_0 , and coincides with the location of zero on the x -axis. Current results (solid black line) are compared to Morgan et al. [55] (dashed lines with symbols).

and higher skin-friction at the wall when thermochemistry is considered in the model. However, the thermochemical model was again simplistic compared to the one included in Mutation++.

In this section, we propose to study the effects of finite-rate chemistry on a steady SBLI at $Ma = 5.92$. A similar case was studied numerically in [23] where the authors used freestream cryogenic conditions of the ACE Hypersonic Wind Tunnel facility at Texas A&M University [72]. In this work, the freestream Mach number and Reynolds number at impinging location Re_{x_0} were kept the same as in [23], while the freestream pressure and temperature have been increased to match the post-shock conditions of a 15° wedge flying at $Ma = 14$ at an altitude of 25 kilometers to promote real-gas effects. The computational domain is a rectangle of size 256×36 reference length units. The reference length is computed from the inflow Reynolds number $Re_{\delta^*} = 9660$ of the original study [23], with the updated freestream conditions, $\tilde{p}_\infty = 60\,967.0$ Pa and $\tilde{T}_\infty = 1110.5$ K, resulting in a similar impinging location and corresponding Reynolds number, $Re_{x_0} = 1.15 \cdot 10^6$. A total of 960 grid points are used in the streamwise direction and 450 in the wall-normal direction, clustered near the wall using Eq. (27). The mesh configuration is specified in Table 3. For this case, both the TPG and CNEQ models are investigated.

The skin friction coefficient and wall pressure for both the TPG and CNEQ models are presented in Fig. 9. The length of the separation bubble is smaller when considering CNEQ effects, in agreement with literature. This is expected with the high concentration of dissociated species in the bubble as seen in Fig. 9c. Just upstream of the reattachment location, the flow exhibits higher skin-friction and wall pressure in the CNEQ case before converging to the same

value as the TPG case after reattachment. These trends are in agreement with the results in [77].

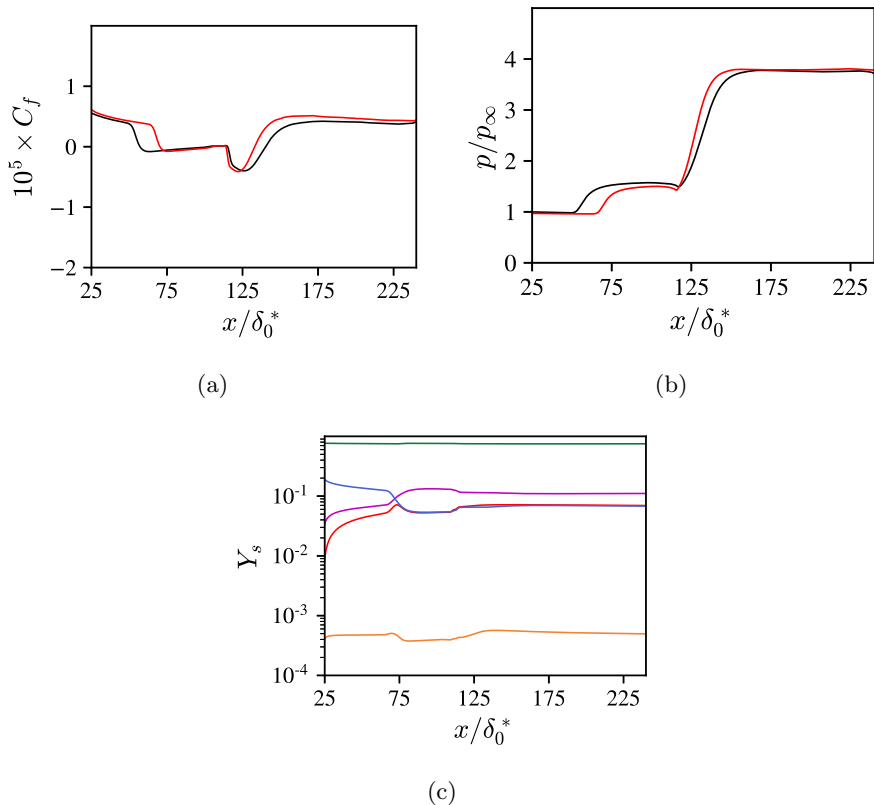


Fig. 9: (a) Skin-friction coefficient and (b) normalized wall pressure stream-wise distribution for the $Ma_\infty = 5.92$ SBLI. Comparison of TPG (black lines) and CNEQ (red lines) results. (c) Mass fraction distributions at the wall for the SBLI in CNEQ. From top to bottom : N_2 , O_2 , O , NO , N .

4.3 Jet in hypersonic crossflow

Normal jet injection into a high-speed crossflow is another canonical flow configuration relevant to a wide range of applications in hypersonic flight. For example, proposed designs of scramjet engines use sonic under-expanded jet injection into a supersonic crossflow to enhance fuel and oxidizer mixing and sustain supersonic combustion. One can also use jet injection into a supersonic/hypersonic crossflow as a reaction control system (RCS) for aerodynamic maneuvering during atmospheric flight [20]. The jet in supersonic crossflow has

also been the subject of a wide range of experimental [2, 14, 64] and numerical studies [9, 33, 61]. The results presented in this section are two-dimensional. Thus, some similarity can be found with the interaction of hypersonic flow over an axisymmetric double cone [76].

The nondimensional parameter that governs the development of flow features is the jet to crossflow momentum ratio J [30], given as,

$$J = \frac{\rho_j U_j^2}{\rho_\infty U_\infty^2}.$$

A case is designed by considering a 15° wedge flying at $Ma = 9$ at an altitude of 25 kilometers. This configuration results in a $Ma = 5$ boundary layer past the nose shock. A self-similar solution with freestream values assigned to post-shock conditions and an adiabatic wall results in $T_{\text{wall}} \approx 4000$ Kelvin (K). This temperature is sufficiently hot to observe intensified dissociation of O_2 into atomic Oxygen and thus can result in a flow in CNEQ. For this case, the CNEQ and TPG models are considered. The freestream and jet thermodynamic conditions are summarized in Table 4. The computational domain is a rectangle of size $32.5D \times 10D$ where $\tilde{D} = 2$ mm is the jet slot width. In the streamwise direction, the inflow starts at $x_0 = 38.5$ and the injection zone is around $x = 52.5$. The inflow and outflow sponges extend for 1 and 2 jet widths, respectively. In the wall-normal direction, grid points are clustered near the wall using Eq. (27), and the last 20 points are used for the sponge. The discretization for this case is specified in Table 5. The simulation is first initialized with an adiabatic condition and the resulting wall temperature is held constant after the jet injection is enforced.

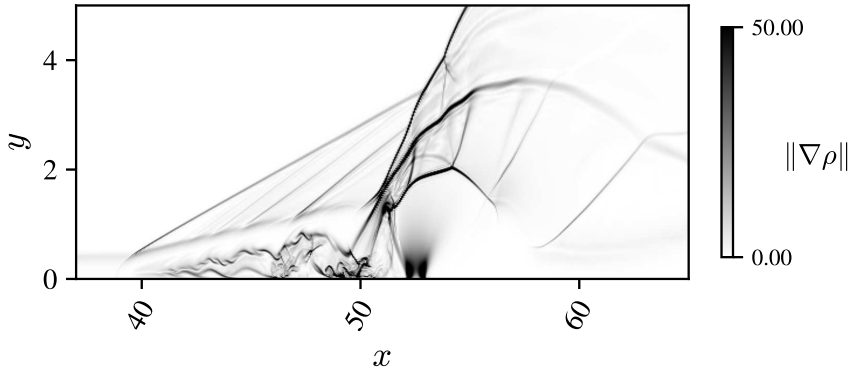
Freestream				Jet			
Ma_∞	$\tilde{p}_\infty [Pa]$	$\tilde{T}_\infty [K]$	Re_D	Ma_{jet}	$\tilde{p}_{\text{jet}}/\tilde{p}_\infty$	$\tilde{T}_{\text{jet}}/T_\infty$	J
5	49800	947	25291	1.0	10.0	1.0	0.4

Table 4: Thermodynamic conditions for the 2D jet in hypersonic crossflow.

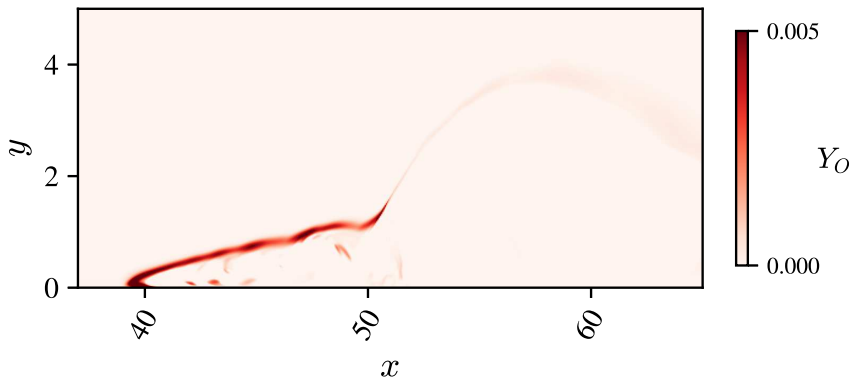
Case	$x_0 - x_1$	$y_0 - y_1$	κ_x	κ_y	N_x	N_y
JISC	38.5 - 71.0	0.0 - 10.0	1.0	0.15	1625	500

Table 5: Mesh configuration for the jet in hypersonic crossflow simulation.

Figure 10a shows a numerical Schlieren image (contours of the density gradient norm) for the jet in crossflow simulation in CNEQ. A number of characteristic flow features are observed. The incoming laminar boundary layer encounters separation upstream of the injection zone, induced by the separation shock created by the upstream unsteady recirculation bubble. A large bow-shock forms in the freestream that diverts the flow. Moreover, a shear



(a)



(b)

Fig. 10: Instantaneous (a) numerical Schlieren and (b) atomic Oxygen mass fraction fields for the sonic jet in $Ma_\infty = 5$ hypersonic crossflow. Jet location is at $x = 52.5$. Configuration parameters may be found in Table 4 and Table 5.

layer emanates from the jet shock structures and the flow past the bow shock induces vortex shedding. This results in a strong coupling between the shock structures, the recirculation bubble, and the shear layer downstream of the injection zone. The structure observed and these interactions are thus similar to those observed for a $Ma = 16$ axisymmetric shock-dominated hypersonic laminar separated flow over a double cone studied by Tumuklu et al. [76]. In their study, a supersonic underexpanded jet is generated through an Edney type IV pattern in the shock-laminar separation bubble. The jet is inherently unsteady and becomes the root of the SBLI instability.

Areas of high concentration of O are observed inside the recirculation bubble in Fig. 10b. In this high-temperature region, atomic Oxygen is produced

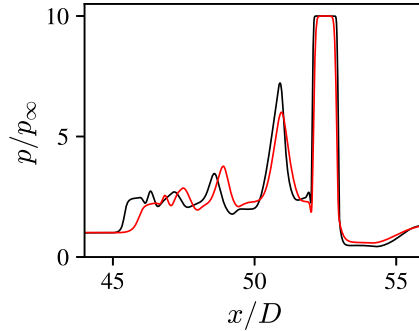


Fig. 11: Instantaneous streamwise distribution of wall pressure for the sonic jet in $Ma_\infty = 5$ crossflow simulation. Comparison of TPG (black lines) and CNEQ (red lines) results.

through the endothermic O_2 dissociation. This reaction absorbs energy from the flow and reduces the size of the recirculation bubble by 10% compared to the TPG simulation Fig. 11. This observation holds for the duration of the instantaneous snapshots considered and is similar to the trend observed in the steady $Ma = 5.92$ SBLI comparison between the TPG and CNEQ models. When CNEQ effects are considered, the adiabatic wall temperature decreases due to endothermic reactions (by about 250 K at the wall) and the boundary layer becomes slightly thicker. The induced cooling effect near the wall leads to a smaller recirculation bubble, and a weaker bow shock. Future work will further analyze the effects of the finite-rate chemistry on the flow field compared to the TPG thermodynamic model, as well as potential changes in the instability characteristics of the flow field in a more realistic 3D configuration.

5 Conclusions

The major challenges posed by the need for space exploration and faster and higher air travel have undoubtedly reinvigorated research interest in applications of hypersonic flow. At such high speed and high enthalpy regimes such as the those encountered during atmospheric (re-)entry or sustained hypersonic cruise, gases do not behave in ways that are predicted by the typical models of computational fluid dynamics (CFD) solvers, and improved models are necessary. In addition, the complex flow scenario results in a large number of phenomena that interact in often non-trivial manners.

In this work, we have presented a computational tool that can accurately simulate flows at hypersonic speed, including high-enthalpy gas effects in the presence of weak and strong shockwaves. We summarize some important milestones in that direction toward our research objective, having verified our numerical tools and tested their application to more complex and physically relevant configurations. The agreement of the presented results is excellent, in

particular in cases where chemistry and shockwaves significantly interact with the flow and physics.

Extensive code verification has been completed, against previous results for reacting boundary layers, SBLI cases, and complex jet injections in high-speed crossflow. The applications have been extended in novel, higher-enthalpy cases where the potential effects of gas thermochemistry are pronounced.

There are a number of directions in which there is significant potential for improvement and extension of the tools' capabilities. First, there are even more accurate options for gas modeling, including state-to-state transitions and taking into account chemistry at the wall (catalicity). Second, there is great interest in extending our results for different gas mixtures, representing atmospheric compositions of celestial objects interesting for space exploration, or for more complex geometry configurations. Third, on the algorithmic side, there are methodologies that can complement, or in some cases even replace, the computationally expensive tasks of the thermochemical model library, using tools from the fields of machine-learning and reduced-order modeling.

Acknowledgments. The authors wish to acknowledge the support of the US Air Force Office of Scientific Research (AFOSR) and the European Office of Aerospace Research and Development (EOARD) under the grant FA9550-18-1-0127, managed by Dr. Sarah Popkin, Dr. Ivett Leyva, and Dr. Douglas Smith. Computational time on National UK Supercomputers has been provided by the UK Turbulence Consortium (UKTC) and Dr. Sylvain Laizet, under the grant EP/R029326/1. Additional computational resources have been made available by the corresponding universities and agencies (Imperial College London, King Abdullah University of Science and Technology (KAUST), Sorbonne University, and the French National Research Center (CNRS)).

Competing interests. The authors report no competing interests. This work was supported by AFOSR and EOARD (Grant FA9550-18-1-0127). Computational time was provided by UKTC (Grant EP/R029326/1). The views and conclusions presented herein are those of the authors and do not represent the views of any of the aforementioned organizations.

Code availability. The Mutation++ library repository is publicly available on <https://github.com/mutationpp/Mutationpp>. The rest of the computational tools developed may be shared by the corresponding author on reasonable request.

Data availability. The datasets generated and/or analyzed during the current study are available from the corresponding author on reasonable request.

References

- [1] J. D. Anderson. *Hypersonic and High-Temperature Gas Dynamics*. American Institute of Aeronautics and Astronautics (AIAA), Washington, DC,

- 3 edition, Apr 2019. ISBN 978-1-62410-514-2. doi: <https://doi.org/10.2514/4.105142>.
- [2] A. Ben-Yakar, M. Mungal, and R. Hanson. Time evolution and mixing characteristics of hydrogen and ethylene transverse jets in supersonic crossflows. *Physics of Fluids*, 18(2):026101, 2006.
- [3] J. J. Bertin and R. M. Cummings. Fifty years of hypersonics: where we've been, where we're going. *Progress in Aerospace Sciences*, 39(6):511–536, 2003. doi: [https://doi.org/10.1016/S0376-0421\(03\)00079-4](https://doi.org/10.1016/S0376-0421(03)00079-4).
- [4] G. V. Candler. Rate effects in hypersonic flows. *Annual Review of Fluid Mechanics*, 51(1):379–402, Jan 2019. ISSN 0066-4189. doi: <https://doi.org/10.1146/annurev-fluid-010518-040258>.
- [5] G. V. Candler and R. W. MacCormack. Computation of weakly ionized hypersonic flows in thermochemical nonequilibrium. *Journal of Thermophysics and Heat Transfer*, 5(3):266–273, Jul 1991. ISSN 0887-8722. doi: <https://doi.org/10.2514/3.260>.
- [6] G. V. Candler, H. B. Johnson, I. Nompelis, P. K. Subbareddy, T. W. Drayna, V. Gidzak, and M. D. Barnhardt. Development of the us3d code for advanced compressible and reacting flow simulations. In *53rd AIAA Aerospace Sciences Meeting*, Jan 2015. ISBN 9781624103438. doi: <https://doi.org/10.2514/6.2015-1893>.
- [7] G. V. Candler, P. K. Subbareddy, and I. Nompelis. CFD methods for hypersonic flows and aerothermodynamics. In E. Josyula, editor, *Hypersonic Nonequilibrium Flows: Fundamentals and Recent Advances*, pages 203–237. American Institute of Aeronautics and Astronautics (AIAA), 2015. doi: <https://doi.org/10.2514/5.9781624103292.0203.0238>.
- [8] M. Carpenter and C. Kennedy. Fourth-order 2n-storage runge-kutta schemes. Technical report, NASA, 07 1994.
- [9] X. Chai, P. S. Iyer, and K. Mahesh. Numerical study of high speed jets in crossflow. *Journal of Fluid Mechanics*, 785:152–188, 2015.
- [10] C. L. Chang, H. Vinh, and M. R. Malik. Hypersonic boundary-layer stability with chemical reactions using pse. In *28th Fluid Dynamics Conference*, pages 1–23, Reston, Virginia, Jun 1997. American Institute of Aeronautics and Astronautics (AIAA). doi: <https://doi.org/10.2514/6.1997-2012>.
- [11] M. Di Renzo and S. Pirozzoli. Htr-1.2 solver: Hypersonic task-based research solver version 1.2. *Computer Physics Communications*, 261: 107733, 2021. ISSN 0010-4655. doi: <https://doi.org/10.1016/j.cpc.2020.107733>.

- [12] M. Di Renzo and J. Urzay. Direct numerical simulation of a hypersonic transitional boundary layer at suborbital enthalpies. *Journal of Fluid Mechanics*, 912:A29, 2021. doi: <https://doi.org/10.1017/jfm.2020.1144>.
- [13] M. Di Renzo, L. Fu, and J. Urzay. Htr solver: An open-source exascale-oriented task-based multi-gpu high-order code for hypersonic aerothermodynamics. *Computer Physics Communications*, 255:107262, 2020. ISSN 0010-4655. doi: <https://doi.org/10.1016/j.cpc.2020.107262>.
- [14] E. Erdem. *Active flow control studies at Mach 5: measurement and computation*. PhD thesis, The University of Manchester, 2011.
- [15] A. Ern and V. Giovangigli. *Multicomponent transport algorithms*, volume 24. Springer Science & Business Media, 1994.
- [16] B. Fiorina and S. Lele. An artificial nonlinear diffusivity method for supersonic reacting flows with shocks. *Journal of Computational Physics*, 222(1):246–264, 2007. ISSN 0021-9991. doi: <https://doi.org/10.1016/j.jcp.2006.07.020>.
- [17] G. H. Furumoto, X. Zhong, and J. C. Skiba. Numerical studies of real-gas effects on two-dimensional hypersonic shock-wave/boundary-layer interaction. *Physics of Fluids*, 9(1):191–210, 1997.
- [18] S. Ghaffari, O. Marxen, G. Iaccarino, and E. S. G. Shaqfeh. Numerical simulations of hypersonic boundary-layer instability with wall blowing. In *48th AIAA Aerospace Sciences Meeting Including the New Horizons Forum and Aerospace Exposition*, 2010. ISBN 9781600867392. doi: <https://doi.org/10.2514/6.2010-706>.
- [19] P. A. Gnoffo, R. N. Gupta, and J. L. Shinn. Conservation equations and physical models for hypersonic air flows in thermal and chemical nonequilibrium. Technical Report 2867, NASA, 1989.
- [20] R. K. Grandhi and A. Roy. Effectiveness of a reaction control system jet in a supersonic crossflow. *Journal of Spacecraft and Rockets*, 54(4): 883–891, 2017.
- [21] G. Groskopf, M. J. Kloker, K. A. Stephani, O. Marxen, and G. Iaccarino. Hypersonic flows with discrete oblique surface roughness and their stability properties. In *Center of Turbulence Research, Proceedings of the Summer Program*, pages 405–422, 2010.
- [22] R. J. Hakkinen, I. Greber, L. Trilling, and S. S. Abarbanel. The interaction of an oblique shock wave with a laminar boundary layer. Technical report, NASA, 1959.

- [23] N. Hildebrand, A. Dwivedi, J. W. Nichols, M. R. Jovanović, and G. V. Candler. Simulation and stability analysis of oblique shock-wave/boundary-layer interactions at Mach 5.92. *Physical Review Fluids*, 3(1):013906, 2018.
- [24] M. S. Holden. Review of aerothermal problems associated with hypersonic flight. In *AIAA Paper*, pages 1–40, Reston, Virginia, Jan 1986. American Institute of Aeronautics and Astronautics (AIAA). doi: <https://doi.org/10.2514/6.1986-267>.
- [25] M. L. Hudson, N. Chokani, and G. V. Candler. Linear stability of hypersonic flow in thermochemical nonequilibrium. *AIAA Journal*, 35(6): 958–964, Jun 1997. ISSN 0001-1452. doi: <https://doi.org/10.2514/2.204>.
- [26] H. B. Johnson and G. V. Candler. Hypersonic boundary layer stability analysis using pse-chem. In *35th AIAA Fluid Dynamics Conference and Exhibit*, Reston, Virginia, Jun 2005. American Institute of Aeronautics and Astronautics (AIAA). ISBN 9781624100598. doi: <https://doi.org/10.2514/6.2005-5023>.
- [27] H. B. Johnson, T. G. Seipp, and G. V. Candler. Numerical study of hypersonic reacting boundary layer transition on cones. *Physics of Fluids*, 10(10):2676–2685, Oct 1998. ISSN 1070-6631. doi: <https://doi.org/10.1063/1.869781>.
- [28] H. B. Johnson, C. Alba, M. D. Bartkowicz, T. W. Drayna, and G. V. Candler. Design optimization of hypersonic vehicles for boundary layer stability. In *26th AIAA Applied Aerodynamics Conference*, pages 1–31, Reston, Virginia, Aug 2008. American Institute of Aeronautics and Astronautics (AIAA). ISBN 978-1-60086-987-7. doi: <https://doi.org/10.2514/6.2008-6221>.
- [29] E. Josyula and P. Vedula. Fundamental fluid transport equations for hypersonic nonequilibrium flows. In E. Josyula, editor, *Hypersonic Nonequilibrium Flows: Fundamentals and Recent Advances*, pages 1–43. American Institute of Aeronautics and Astronautics (AIAA), 2015. doi: <https://doi.org/10.2514/5.9781624103292.0001.0044>.
- [30] A. R. Karagozian. The jet in crossflow. *Physics of Fluids*, 26(10):1–47, 2014.
- [31] E. Katzer. On the lengthscales of laminar shock/boundary-layer interaction. *Journal of Fluid Mechanics*, 206:477–496, 1989.
- [32] S. Kawai and S. K. Lele. Localized artificial diffusivity scheme for discontinuity capturing on curvilinear meshes. *Journal of Computational Physics*, 229:9498–9526, 2008.

- [33] S. Kawai and S. K. Lele. Large-eddy simulation of jet mixing in supersonic crossflows. *AIAA Journal*, 48(9):2063–2083, 2010.
- [34] S. Kawai and S. K. Shankar, Santhosh K. and Lele. Assessment of localized artificial diffusivity scheme for large-eddy simulation of compressible turbulent flows. *Journal of Computational Physics*, 227:1739–1762, 2010.
- [35] C. A. Kennedy, M. H. Carpenter, and R. Lewis. Low-storage, explicit runge–kutta schemes for the compressible navier–stokes equations. *Applied Numerical Mathematics*, 35(3):177–219, 2000. ISSN 0168-9274. doi: [https://doi.org/10.1016/S0168-9274\(99\)00141-5](https://doi.org/10.1016/S0168-9274(99)00141-5).
- [36] S. K. Lele. Compact finite difference schemes with spectral-like resolution. *Journal of Computational Physics*, 103(1):16–42, 1992. ISSN 0021-9991. doi: [https://doi.org/10.1016/0021-9991\(92\)90324-R](https://doi.org/10.1016/0021-9991(92)90324-R).
- [37] I. A. Leyva. The relentless pursuit of hypersonic flight. *Physics Today*, 70(11):30–36, Nov 2017. ISSN 00319228. doi: <https://doi.org/10.1063/PT.3.3762>.
- [38] M. R. Malik. Prediction and control of transition in supersonic and hypersonic boundary layers. *AIAA Journal*, 27(11):1487–1493, 1989. ISSN 00011452. doi: <https://doi.org/10.2514/3.10292>.
- [39] M. R. Malik and E. C. Anderson. Real gas effects on hypersonic boundary-layer stability. *Physics of Fluids A: Fluid Dynamics*, 3(5):803–821, May 1991. ISSN 0899-8213. doi: <https://doi.org/10.1063/1.858012>.
- [40] M. R. Malik, T. A. Zang, and D. M. Bushnell. Boundary layer transition in hypersonic flows. In *AIAA 2nd International Aerospace Planes Conference, 1990*, pages 1–21, Reston, Virginia, Oct 1990. American Institute of Aeronautics and Astronautics (AIAA). doi: <https://doi.org/10.2514/6.1990-5232>.
- [41] A. Mani, J. Larsson, and P. Moin. Suitability of artificial bulk viscosity for large-eddy simulation of turbulent flows with shocks. *Journal of Computational Physics*, 228(19):7368–7374, 2009. ISSN 0021-9991. doi: <https://doi.org/10.1016/j.jcp.2009.06.040>.
- [42] O. Marxen and G. Iaccarino. An immersed boundary method for numerical simulations of boundary layers with roughness. Technical report, Stanford University, 2008.
- [43] O. Marxen, G. Iaccarino, and E. S. G. Shaqfeh. Disturbance evolution in a Mach 4.8 boundary layer with two-dimensional roughness-induced separation and shock. *Journal of Fluid Mechanics*, 648:435–469, 2010. ISSN 00221120. doi: <https://doi.org/10.1017/S0022112009992758>.

- [44] O. Marxen, T. E. Magin, G. Iaccarino, and E. S. G. Shaqfeh. Hypersonic boundary-layer instability with chemical reactions. In *48th AIAA Aerospace Sciences Meeting Including the New Horizons Forum and Aerospace Exposition*, Reston, Virginia, Jan 2010. American Institute of Aeronautics and Astronautics (AIAA). ISBN 9781600867392. doi: <https://doi.org/10.2514/6.2010-707>.
- [45] O. Marxen, T. E. Magin, G. Iaccarino, and E. S. G. Shaqfeh. A high-order numerical method to study hypersonic boundary-layer instability including high-temperature gas effects. *Physics of Fluids*, 23(8):084108, Aug 2011. ISSN 10706631. doi: <https://doi.org/10.1063/1.3614526>.
- [46] O. Marxen, T. E. Magin, E. S. G. Shaqfeh, and G. Iaccarino. A method for the direct numerical simulation of hypersonic boundary-layer instability with finite-rate chemistry. *Journal of Computational Physics*, 255:572–589, 2013. ISSN 10902716. doi: <https://doi.org/10.1016/j.jcp.2013.07.029>.
- [47] O. Marxen, G. Iaccarino, and T. E. Magin. Direct numerical simulations of hypersonic boundary-layer transition with finite-rate chemistry. *Journal of Fluid Mechanics*, 755:35–49, Sep 2014. ISSN 14697645. doi: <https://doi.org/10.1017/jfm.2014.344>.
- [48] O. Marxen, G. Iaccarino, and E. S. G. Shaqfeh. Nonlinear instability of a supersonic boundary layer with two-dimensional roughness. *Journal of Fluid Mechanics*, 752(4):497–520, 2014. ISSN 14697645. doi: <https://doi.org/10.1017/jfm.2014.266>.
- [49] F. Miró Miró and F. Pinna. Linear stability analysis of a hypersonic boundary layer in equilibrium and non-equilibrium. In *47th AIAA Fluid Dynamics Conference*, Reston, Virginia, Jun 2017. American Institute of Aeronautics and Astronautics (AIAA). ISBN 978-1-62410-500-5. doi: <https://doi.org/10.2514/6.2017-4518>.
- [50] F. Miró Miró and F. Pinna. Effect of uneven wall blowing on hypersonic boundary-layer stability and transition. *Physics of Fluids*, 30(8), 2018. ISSN 10897666. doi: <https://doi.org/10.1063/1.5043353>.
- [51] F. Miró Miró and F. Pinna. On decoupling ablation effects on boundary-layer stability and transition. In *AIAA Aviation 2019 Forum*, Reston, Virginia, Jun 2019. American Institute of Aeronautics and Astronautics (AIAA). ISBN 978-1-62410-589-0. doi: <https://doi.org/10.2514/6.2019-2854>.
- [52] F. Miró Miró, E. S. Beyak, D. Mullen, F. Pinna, and H. L. Reed. Ionization and dissociation effects on hypersonic boundary-layer stability. In *31st Congress of the International Council of the Aeronautical Sciences*

(*ICAS*) 2018, 2018.

- [53] F. Miró Miró, F. Pinna, E. S. Beyak, P. Barbante, and H. L. Reed. Diffusion and chemical non-equilibrium effects on hypersonic boundary-layer stability. In *2018 AIAA Aerospace Sciences Meeting*, Reston, Virginia, Jan 2018. American Institute of Aeronautics and Astronautics (AIAA). ISBN 978-1-62410-524-1. doi: <https://doi.org/10.2514/6.2018-1824>.
- [54] F. Miró Miró, P. Dehairs, F. Pinna, M. Gkolia, D. Masutti, T. Regert, and O. Chazot. Effect of wall blowing on hypersonic boundary-layer transition. *AIAA Journal*, 57(4):1567–1578, Apr 2019. ISSN 0001-1452. doi: <https://doi.org/10.2514/1.J057604>.
- [55] B. Morgan, S. Kawai, and S. Lele. Large-eddy simulation of an oblique shock impinging on a turbulent boundary layer. In *40th Fluid Dynamics Conference and Exhibit*, page 4467, 2010.
- [56] S. Nagarajan. *Leading edge effects in bypass transition*. PhD thesis, Stanford University, 2004.
- [57] S. Nagarajan, S. K. Lele, and J. H. Ferziger. A robust high-order compact method for large eddy simulation. *Journal of Computational Physics*, 191(2):392–419, 2003.
- [58] J. W. Nichols and G. V. Candler. Input-output analysis of complex hypersonic boundary layers. In *AIAA Scitech 2019 Forum*, pages 1–11, Reston, Virginia, Jan 2019. American Institute of Aeronautics and Astronautics (AIAA). ISBN 978-1-62410-578-4. doi: <https://doi.org/10.2514/6.2019-1383>.
- [59] D. Passiatore, L. Sciacovelli, P. Cinnella, and G. Pascazio. Finite-rate chemistry effects in turbulent hypersonic boundary layers: A direct numerical simulation study. *Phys. Rev. Fluids*, 6:054604, May 2021. doi: <https://doi.org/10.1103/PhysRevFluids.6.054604>.
- [60] D. Passiatore, L. Sciacovelli, P. Cinnella, and G. Pascazio. Thermochemical non-equilibrium effects in turbulent hypersonic boundary layers. *Journal of Fluid Mechanics*, 941:A21, 2022. doi: <https://doi.org/10.1017/jfm.2022.283>.
- [61] D. Peterson, P. Subbareddy, and G. Candler. Assessment of synthetic inflow generation for simulating injection into a supersonic crossflow. In *14th AIAA/AHI Space Planes and Hypersonic Systems and Technologies Conference*, page 8128, 2006.
- [62] F. Pinna and F. Miró Miró. Numerical modeling of continuous blowing surface in hypersonic boundary layers. In *7th European Conference for*

- Aeronautics and Aerospace Sciences (EUCASS) 2017*, 2017. doi: <https://doi.org/10.13009/EUCASS2017-68>.
- [63] J. D. Ramshaw. Self-consistent effective binary diffusion in multicomponent gas mixtures. *Journal of Non-Equilibrium Thermodynamics*, 1990.
- [64] J. G. Santiago and J. C. Dutton. Velocity measurements of a jet injected into a supersonic crossflow. *Journal of propulsion and power*, 13(2):264–273, 1997.
- [65] T. Sayadi, C. W. Hamman, and P. Moin. Direct numerical simulation of complete H-type and K-type transitions with implications for the dynamics of turbulent boundary layers. *Journal of Fluid Mechanics*, 724: 480–509, 2013.
- [66] J. D. Schmisser. Hypersonics into the 21st century: A perspective on afosr-sponsored research in aerothermodynamics. *Progress in Aerospace Sciences*, 72:3–16, Jan 2015. ISSN 03760421. doi: <https://doi.org/10.1016/j.paerosci.2014.09.009>.
- [67] S. P. Schneider. Summary of hypersonic boundary-layer transition experiments on blunt bodies with roughness. *Journal of Spacecraft and Rockets*, 45(6):1090–1105, 2008. ISSN 00224650. doi: <https://doi.org/10.2514/1.37431>.
- [68] L. Sciacovelli, D. Passiatore, P. Cinnella, and G. Pascazio. Assessment of a high-order shock-capturing central-difference scheme for hypersonic turbulent flow simulations. *Computers & Fluids*, 230:105134, 2021. ISSN 0045-7930. doi: <https://doi.org/10.1016/j.compfluid.2021.105134>.
- [69] J. B. Scoggins. *Development of numerical methods and study of coupled flow, radiation, and ablation phenomena for atmospheric entry*. PhD thesis, Université Paris-Saclay and von Karman Institute for Fluid Dynamics, 2017.
- [70] J. B. Scoggins and T. E. Magin. Development of mutation++: Multi-component thermodynamic and transport properties for ionized plasmas written in C++. In *11th AIAA/ASME Joint Thermophysics and Heat Transfer Conference*. American Institute of Aeronautics and Astronautics (AIAA), 2014. ID: AIAA 2014-2966.
- [71] J. B. Scoggins, V. Leroy, G. Bellas-Chatzigeorgis, B. Dias, and T. E. Magin. Mutation++: Multicomponent thermodynamic and transport properties for ionized gases in c++. *SoftwareX*, 12:100575, 2020. ISSN 2352-7110. doi: <https://doi.org/10.1016/j.softx.2020.100575>.

- [72] M. Semper, B. Pruski, and R. Bowersox. Freestream turbulence measurements in a continuously variable hypersonic wind tunnel. In *50th AIAA Aerospace Sciences Meeting including the New Horizons Forum and Aerospace Exposition*, page 732, 2012.
- [73] P. Shrestha and G. V. Candler. Direct numerical simulation of high-speed transition due to roughness elements. *Journal of Fluid Mechanics*, 868: 762–788, Jun 2019. ISSN 0022-1120. doi: <https://doi.org/10.1017/jfm.2019.179>.
- [74] P. K. Subbareddy, M. D. Bartkowicz, and G. V. Candler. Direct numerical simulation of high-speed transition due to an isolated roughness element. *Journal of Fluid Mechanics*, 748:848–878, Jun 2014. ISSN 0022-1120. doi: <https://doi.org/10.1017/jfm.2014.204>.
- [75] V. Theofilis, S. Pirozzoli, and P. Martin. Special issue on the fluid mechanics of hypersonic flight. *Theoretical and Computational Fluid Dynamics*, 36(1):1–8, 2022. doi: <https://doi.org/10.1007/s00162-022-00605-2>.
- [76] O. Tumuklu, V. Theofilis, and D. A. Levin. On the unsteadiness of shock–laminar boundary layer interactions of hypersonic flows over a double cone. *Physics of Fluids*, 30(10):106111, 2018.
- [77] P. S. Volpiani. Numerical strategy to perform direct numerical simulations of hypersonic shock/boundary-layer interaction in chemical nonequilibrium. *Shock Waves*, 31(4):361–378, 2021.
- [78] V. Wartemann, A. Wagner, R. Wagnild, F. Pinna, F. Miró Miró, and H. Tanno. Code comparison on hypersonic high enthalpy transitional boundary layers. In *2018 AIAA Aerospace Sciences Meeting*, pages 1–14, Reston, Virginia, Jan 2018. American Institute of Aeronautics and Astronautics (AIAA). ISBN 978-1-62410-524-1. doi: <https://doi.org/10.2514/6.2018-0351.c1>.
- [79] V. Wartemann, A. Wagner, R. Wagnild, F. Pinna, F. Miró Miró, H. Tanno, and H. B. Johnson. High-enthalpy effects on hypersonic boundary-layer transition. *Journal of Spacecraft and Rockets*, 56(2): 347–356, Mar 2019. ISSN 0022-4650. doi: <https://doi.org/10.2514/1.A34281>.
- [80] M. J. Wright, G. V. Candler, and D. Bose. Data-parallel line relaxation method for the navier-stokes equations. *AIAA Journal*, 36(9):1603–1609, Sep 1998. ISSN 00011452. doi: <https://doi.org/10.2514/2.586>.
- [81] L. Zanus, F. Miró Miró, and F. Pinna. Parabolized stability analysis of chemically reacting boundary layer flows in equilibrium conditions. In *7th European Conference for Aeronautics and Aerospace Sciences (EUCASS)*

2017, pages 1–15, 2017. doi: <https://doi.org/10.13009/EUCASS2017-288>.

- [82] L. Zanus, F. Miró Miró, and F. Pinna. Nonlinear parabolized stability analysis of hypersonic flows in presence of curvature effects. In *2018 AIAA Aerospace Sciences Meeting*, Reston, Virginia, Jan 2018. American Institute of Aeronautics and Astronautics (AIAA). ISBN 978-1-62410-524-1. doi: <https://doi.org/10.2514/6.2018-2087>.
- [83] L. Zanus, F. Miró Miró, and F. Pinna. Weak non-parallel effects on chemically reacting hypersonic boundary layer stability. In *AIAA Aviation 2019 Forum*, pages 1–20, Reston, Virginia, Jun 2019. American Institute of Aeronautics and Astronautics (AIAA). ISBN 978-1-62410-589-0. doi: <https://doi.org/10.2514/6.2019-2853>.